

Background-subtracted Solar Activity Maps

C. Denker¹ · M. Verma¹

Version: 25 February 2022
© Springer Science+Business Media Dordrecht 2019

Abstract We introduce the concept of a *Background-subtracted Solar Activity Map* (BaSAM) as a new quantitative tool to assess and visualize the temporal variation of the photospheric magnetic field and the UV $\lambda 160$ nm intensity. The method utilizes data of the *Solar Dynamics Observatory* (SDO) and is applicable to both full-disk observations and regions-of-interest. We illustrate and discuss the potential of BaSAM resorting to datasets representing solar minimum and maximum conditions: (1) Contributions of quiet-Sun magnetic fields, *i.e.* the network and (decaying) plage, to solar activity can be better determined when their variation is measured with respect to the background given by “deep” magnetograms. (2) Flaring and intermittent brightenings are easily appraised in BaSAMs of the UV intensity. (3) Both magnetic-field and intensity variations demonstrated that the flux system of sunspots is well connected to the surrounding supergranular cells. In addition, producing daily full-disk BaSAMs for the entire mission time of SDO provides a unique tool to analyze solar cycle variations, showing how vigorous or frail are the variations of magnetic-field and intensity features.

Keywords: Active Regions · Solar Cycle, Observations · Magnetic Fields, Photosphere · Chromosphere · Instrumentation and Data Management

1. Introduction

The long-term variation of the solar magnetic field was extensively studied using synoptic maps created from full-disk magnetograms. Gaizauskas *et al.* (1983) utilized synoptic maps of photospheric magnetic fields using the Kitt Peak National Observatory’s full-disk photospheric magnetograms for the ascending phase of solar cycle 21. In their synoptic maps, they followed the “complexes of activity” (Bumba and Howard, 1965) and noticed that these complexes of activity formed within a month, maintaining themselves by addition of fresh magnetic flux for 3–6 solar rotations. de Toma, White, and Harvey (2000) carried out a similar study but for the ascending phase of solar cycle 23. In addition to using magnetic synoptic charts, they used time-series of the

✉ C. Denker
cdenker@aip.de

¹ Leibniz-Institut für Astrophysik Potsdam (AIP), An der Sternwarte 16, 14482 Potsdam, Germany

10.7 cm radio flux, sunspot numbers, and the Mg II chromospheric index for determining the origin of the two activity minima in 1996. The synoptic charts provided the details of the activity belt and activity nests, indicating preferred longitude bands where activity reoccurred. The properties of global magnetic evolution are, for example, needed to constrain flux transport dynamo models.

With the advent of digital imaging, time-series analysis became an important tool to obtain information about the variation, dynamics, and evolution of solar features. For example, extracting the intensity along a spatial slice at a given time from a time-sequence yields so-called space-time or time-slice diagrams. They are commonly used, *e.g.* to infer information about exploding granules (Title *et al.*, 1986), to detect oscillatory motions of bright points in continuum images (Wang *et al.*, 1995), to compare magnetic flux measurements derived from near-infrared and visible spectropolarimetric observations (Lin and Rimmele, 1999), and to determine the divergence of the horizontal velocity field (Shine, Simon, and Hurlburt, 2000). More recently, Verma *et al.* (2016) followed the complete evolution of an active region using space-time diagrams based on synoptic line-of-sight (LOS) magnetograms. Various other time-series analysis methods are widely used and implemented fostering a better understanding the physical processes on the solar surface, *e.g.* difference maps (see Aschwanden *et al.*, 1999, for solar active region loops), sliding averages (see Rouppe van der Voort *et al.*, 2003, for umbral flashes and running penumbral waves), time-lag maps (see Viall and Klimchuk, 2012, for coronal loops), decorrelation times for lifetimes of flows and of active region magnetic structures (Welsch *et al.*, 2012; Verma and Denker, 2012), and spatial correlation analysis (see Verma and Denker, 2011, for an adaptation of *Local Correlation Tracking* (LCT)). Although many of these methods are versatile, not all of them are suitable for determining the global or large-scale evolution of solar intensity and magnetic field.

To visualize variations of the magnetic field in and around a decaying sunspot, Verma *et al.* (2012) presented a map of temporal variations in the magnetic flux above and below the local background, *i.e.* the long-term average of the magnetic field. Analyzing a 12-hour time-series of LOS magnetograms revealed regions of enhanced activity. A spoke-like structure was discovered in the background-subtracted variation map, which indicated moving magnetic features (MMFs) emanating from the photometric sunspot border, traveling along preferential paths, and reaching all the way to the surrounding supergranular boundary. Kummerow (2015) and Verma, Kummerow, and Denker (2018) extended this work by computing a large sample of these background-subtracted variation maps for various sunspots complemented by time-series of UV images. While these studies were focused on a specific region-of-interest (ROI) covering individual sunspots, we will carry our initial work forward and propose in this study efficient tools to infer properties of the global magnetic field and the solar activity in general.

In Beauregard, Verma, and Denker (2012), we extended our implementation of LCT (Verma and Denker, 2011), originally developed by November and Simon (1988), to full-disk continuum images, and we used the *Differential Affine Velocity Estimator* (DAVE, Schuck, 2005, 2006) to derive flux transport velocities from full-disk magnetograms. Large volumes of data are involved in computing horizontal flow fields. Having these three-dimensional data cubes in hand (two spatial and the time coordinate) motivated us to explore the temporal variation of magnetic and UV activity for each pixel in the field-of-view (FOV), complementing optical flow techniques. All

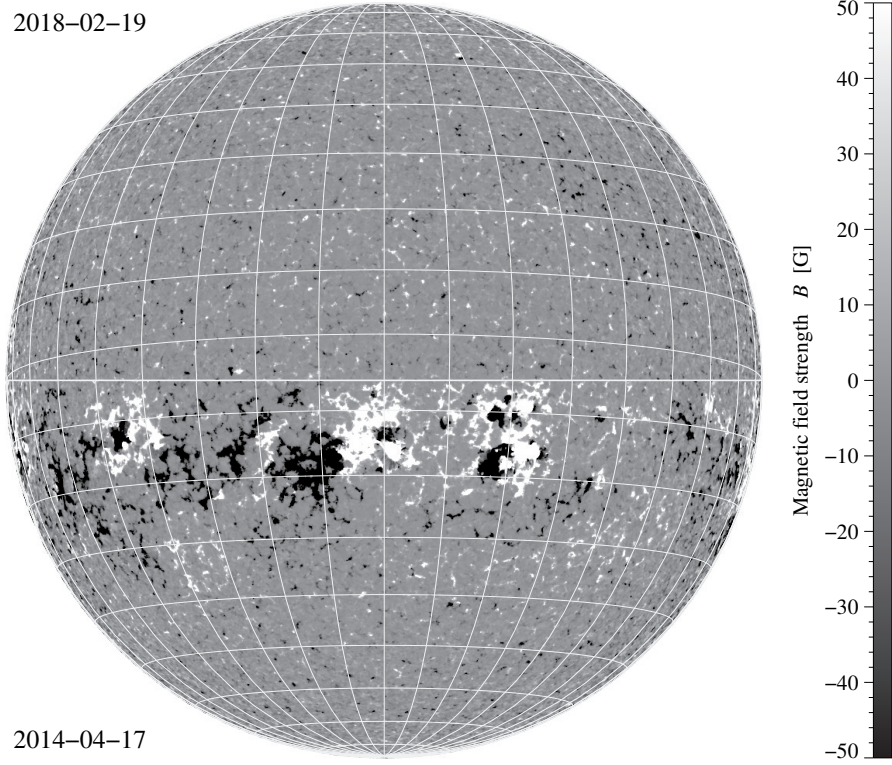


Figure 1. Composite of two deep full-disk magnetograms $\langle B \rangle_{16h}$ depicting solar minimum (*top*) and maximum (*bottom*) activity levels on 2018 February 19 and 2014 April 17, respectively.

methods mentioned above deal with images and magnetograms one way or the other. The purpose is to extract as much information as possible regarding solar activity and evolution of solar features from these kinds of datasets. In the present study, we extend our previous work related to the variation of magnetic fields and UV intensity (*e.g.* Verma *et al.*, 2012; Verma, Kummerow, and Denker, 2018) and formally introduce the method as *Background-subtracted Solar Activity Map* (BaSAM).

In the following, we describe typical datasets (Section 2), present briefly the straightforward, though computationally extensive, implementation of our method (Section 3), show results for full-disk and ROI data (Section 4), and discuss some of the common applications (Section 5).

2. Observations

One day during solar maximum (2014 April 17) and another day during the declining phase (2018 February 19) of solar cycle 24 were selected for case studies to illustrate the potential of BaSAM (see Figures 1 and 2). In addition, a two-hour time window was selected for each day of the *Solar Dynamics Observatory* (SDO, Pesnell, Thompson, and Chamberlin, 2012) mission so far (2010 May 1 – 2018 July 31), which resulted in a

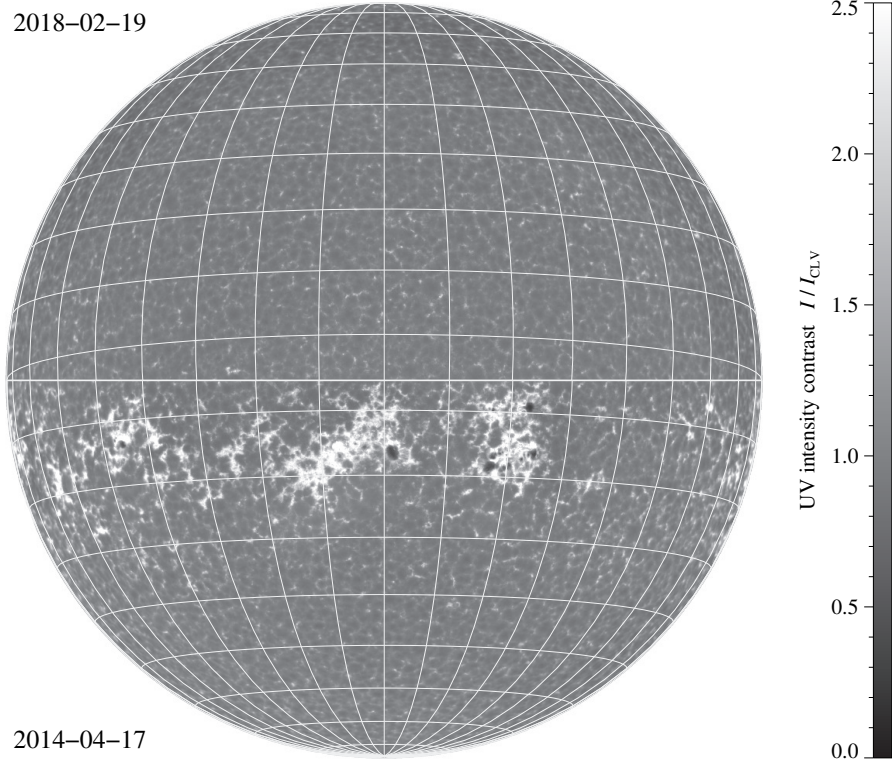


Figure 2. Composite of two full-disk images of the limb-darkening corrected, normalized UV intensity $\langle I \rangle_{16h}$.

long-duration dataset containing about 3000 observing days. This long-duration dataset is the basis for the derivation of BaSAM indices tracing solar activity.

The activity maps are based on full-disk datasets of two SDO instruments, *i.e.* the *Helioseismic and Magnetic Imager* (HMI, Scherrer *et al.*, 2012; Schou *et al.*, 2012) and the *Atmospheric Imaging Assembly* (AIA, Lemen *et al.*, 2012). Time-series of line-of-sight (LOS) magnetograms and UV $\lambda 160$ nm images serve as input for the case studies, which cover a period of ± 8 hours around 12:00 UT. The cadence of HMI and AIA data are $\Delta t = 45$ s and 24 s, respectively. Thus, 1280 magnetograms and 2400 UV images are potentially available during the time period of $\Delta T = 16$ h. However, on 2018 February 19, only 1157 magnetograms were retrieved, *i.e.* no magnetic field data were available for the time period from 06:42 to 08:08 UT. In the UV time-series only about 10 images are missing, which is negligible. All magnetograms and UV images in the time-series are compensated for differential rotation using 12:00 UT as time reference. The long-duration dataset comprises only magnetograms, which cover a period of ± 1 hour around 12:00 UT. However, eclipse seasons of SDO, when the view towards the Sun is obstructed, cause gaps in the time-series. These gaps were filled with two-hour times-series of magnetograms that are as close in time to 12:00 UT as possible. While the bulk processing of the daily magnetogram data can be automated, some manual interaction was needed to fill the gaps caused by the eclipse seasons.

The differential rotation is corrected using the standard mapping routines of the SolarSoftWare library (SSW, Freeland and Handy, 1998), which implements by default the differential rotation rate of small magnetic features (Howard, Harvey, and Forgach, 1990). Compared to other differential rotation laws, for example for different solar features or derived with other methods, the largest error is expected at the central meridian, where projection effects are minimal. For a rough error estimate, the default differential rotation rate was compared to that given by Snodgrass and Ulrich (1990), which is based on photospheric Doppler velocity features. In the temporal sampling window of one hour, the error is less than one third of a pixel, which is negligible. Even for the longest sampling window of eight hours, the error is only about 2.5 pixels. Hence, these mismatch errors may lead to some diffusion of the magnetic flux or intensity, which however can be safely neglected.

Co-adding all magnetograms subsequent to differential-rotation correction yields the deep magnetogram in Figure 1, where the magnetic field strength B was corrected for the cosine of the heliocentric angle $\mu = \cos \theta$. This first-order correction ensures that magnetic fields near the limb and disk center are equally well represented. However, in difference images, this straightforward correction may lead to complications because small differences will be strongly enhanced in proximity to the solar limb. The deep full-disk magnetogram is a composite of the Sun’s quiet northern hemisphere on 2018 February 1 and the very active southern hemisphere on 2014 April 17. The northern hemisphere on 2014 April 17 is also very active, *i.e.* it contains a large number of active regions, which are however not as prominent as those in the southern hemisphere. This type of composite display allows us to directly compare activity levels at solar minimum and maximum. The selected threshold of ± 50 G for the deep magnetogram enhances both the network magnetic fields and the active plage regions. The superposed Stonyhurst grid represents solar longitude and latitude in 10° increments for both observing days at 12:00 UT. The solid horizontal line does not mark the solar equator, it just separates the northern and southern hemispheres. All full-disk data in the following sections adhere to the same display style.

A long-integration UV intensity composite map was created using a similar procedure. However, we first determined the center-to-limb variation (CLV) on 2018 February 19 by fitting a 4th-order polynomial in μ (see Denker *et al.*, 1999, for a description of the procedure), when the solar activity was very low, and divided the UV intensity map by a two-dimensional representation of the CLV. The same CLV correction was applied to the UV intensity map on 2014 April 17 after appropriate scaling, taking into account variations of the disk-center intensity. Thus, the composite of two full-disk images shown in Figure 2 displays the UV intensity normalized with respect to the local quiet-Sun intensity. The imprint of the supergranulation, *i.e.* the bright network (“orange peel pattern”) is much more pronounced in this normalized UV image as compared to the deep magnetograms. In any case, even though some structural contents is lost when taking the long-duration averages, some solar features will be enhanced so that this type of image processing has merits of its own. Apart from that further processing of time-series data comprised of magnetograms and UV images reveals additional information (see Section 4).

3. Background-subtracted Solar Activity Maps

The availability of high-cadence synoptic full-disk data with a moderate spatial resolution of about one second of arc is the prerequisite for our method to assess variations in magnetic field and UV/EUV imaging data. Instead of exploring the rms-contrast of two-dimensional surface data, we explore the temporal variation for each pixel on the solar disk. Thus, we implemented BaSAM as the mean absolute deviation of a time-series calculated for each pixel on the solar disk. In principle, the method can also be based on rms-measurements. However, stronger variations will receive a higher weight in this case, which is undesirable when computing activity indices. In general, the background-subtracted variation of a quantity S with time, for example that of the magnetic field strength B or the UV intensity I , is computed according to

$$\langle |S - \langle S \rangle| \rangle = \frac{1}{N} \sum_{i=1}^N |S(t_i) - \langle S \rangle| \quad \text{with} \quad \langle S \rangle = \frac{1}{N} \sum_{i=1}^N S(t_i). \quad (1)$$

The individual images in a time-series are given by $S(t_i)$. The notation on the left-hand side of the equations is just shorthand for the mathematical formalism on the right-hand side. The expression $\langle |B - \langle B \rangle| \rangle_{2h}$, for example, refers to a BaSAM based on a time-series with a duration of $\Delta T = 2$ h containing typically $N = 160$ magnetograms (Figure 3), whereas $\langle B \rangle_{16h}$ is an abbreviation for a sixteen-hour deep magnetogram (Figure 1). Since the cadence of the UV images is about two times higher, the UV BaSAM $\langle |I - \langle I \rangle| \rangle_{2h}$ is based on $N = 300$ images (Figure 4).

In Equation 1, the local background $\langle S \rangle$, which was computed just once, across the entire time-series, may be replaced by a simple sliding average

$$\langle S \rangle^M = \frac{1}{M+1} \sum_{j=i-M/2}^{j=i+M/2} S(t_j), \quad (2)$$

which has to be updated for each time step t_i in order to compute the absolute difference $|S(t_i) - \langle S \rangle|$ in Equation 1. Thus, $\langle |I - \langle I \rangle| \rangle_{16h}^{30\min}$ refers to a 16-hour BaSAM of the UV intensity that was computed with a 30-minute sliding average. Using sliding averages is advantageous, for example, when studying transient events such as flares. The notation in Equation 2 does not address how to compute the sliding averages at the beginning and end of the time-series. We simply opted for computing the sliding average based on images contained within a time-series of given duration, *i.e.* no images before or after the time-series were included in the average. Thus, the duration of the sliding average is shorter at the beginning and end of the times-series, which is however negligible as long as the duration of the sliding average is much shorter than the duration of the time-series.

Photon noise is the dominant noise term for magnetograms and UV images. Thus, the CLV introduces a systematic increase of the noise from disk center to the limb. Table 1 in Couvidat *et al.* (2016) lists an uncertainty of 7 G for the 45-second cadence, LOS magnetograms near disk center, which increases by a factor of about 1.7 at the limb. Relevant information on the wavelength dependent solar limb darkening is given by Pierce and Slaughter (1977) for HMI magnetograms and by Pierce, Slaughter, and Weinberger (1977) for AIA UV images, which can be used to compute the noise level

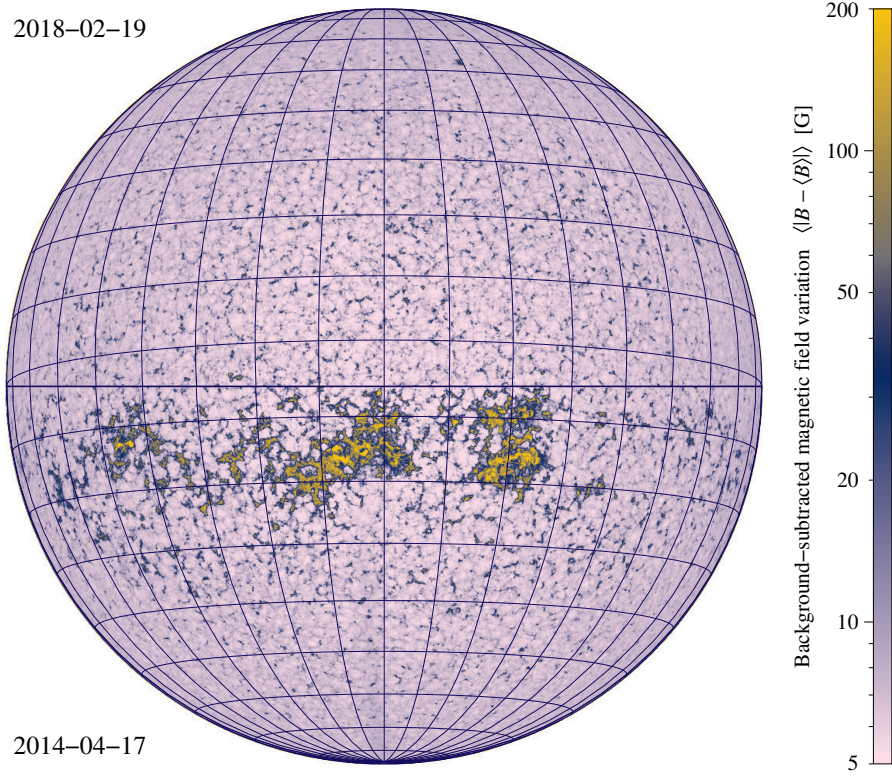


Figure 3. Composite of two full-disk BaSAMs $\langle |B - \langle B \rangle| \rangle_{16h}$ (logarithmic display) corresponding to Figure 1.

as a function of heliocentric angle. In addition, solar differential rotation shifts the spectral line profile across the HMI filter positions, which results in an additional noise component that increases with distance from the central meridian. Since the noise in $\langle S \rangle$ is significantly lower than in $S(t_i)$, the latter will dominate $|S(t_i) - \langle S \rangle|$, which leads to a basal noise floor in the summation of Equation 1. Moreover, magnetic BaSAMs and deep magnetograms are governed by the same photon statistics based on the number of “integrated” single magnetograms. The quiet-Sun magnetograms in Figure 5 visualize the noise being present in single and deep magnetograms, respectively. The magnetograms were clipped at different thresholds ensuring that about 10% of the pixels are saturated at the threshold. The single magnetogram only shows the strongest network elements, whereas the 2-hour averaged magnetogram shows both strong network and weak internetwork magnetic fields. The latter can lead to an additional basal component in magnetic BaSAMs based on very deep magnetograms (see Figure 5c), where the contributions by weak internetwork fields are washed out over the 16-hour averaging period.

In case studies, ROI processing is often more appropriate when focusing on objects such as pores, sunspots, or more complex active regions. However, additional processing steps may be necessary: (1) Proper motions related to active region evolution will be

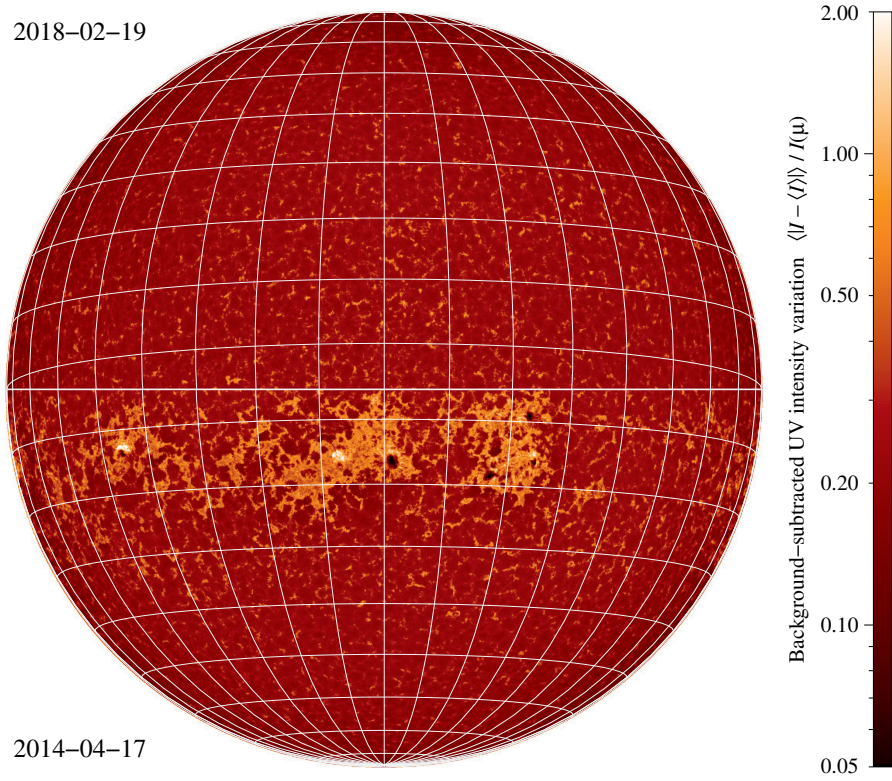


Figure 4. Composite of two full-disk BaSAMS $\langle |I - \langle I \rangle| \rangle_{16h} / I(\mu)$ (logarithmic display) corresponding to Figure 2.

present in time-series. The cross-correlation between single magnetograms and images and their respective long-duration averages identifies these residual drifts, which are subsequently removed. (2) Resampling on a regular grid with an equidistant spacing will be advantageous if the same data are used to determine horizontal proper motions, which ensures that the sampling window to derive velocity vectors covers equal areas. (3) If the ROI is located in proximity to the solar limb, geometric corrections for the magnetic field inclination or photometric corrections for the CLV will be expedient. The data processing steps in these situations essentially follow the procedures elaborated in Verma and Denker (2011) and Beauregard, Verma, and Denker (2012). Thus, the choice of additional processing steps is driven by the specific science case. Only in statistical or comparative studies standardized processing steps are required.

4. Results

Various parameters affect the appearance of BaSAMS. Thus, they must be carefully chosen according to the science case. In the following, we provide a parameter study, investigating the impact of the duration for which BaSAMS are computed and of the duration of the sliding averages. We selected an ROI in the northern hemisphere (not

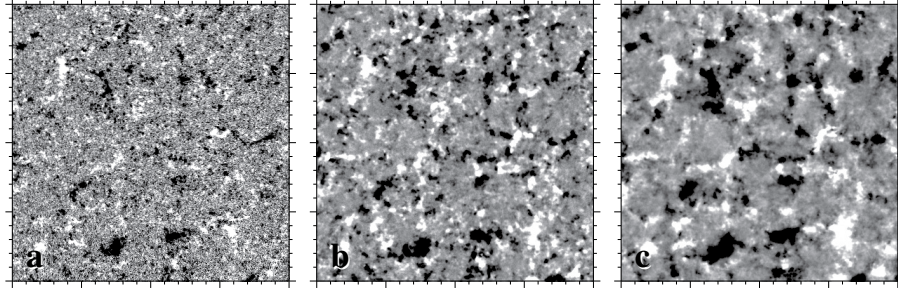


Figure 5. Quiet-Sun magnetograms ($200'' \times 200''$) taken at disk center at around 12:00 UT on 2018 February 19: (a) single, (b) 2-hour average, and (c) 16-hour average magnetogram, respectively. The magnetograms were scaled such that 10% of the pixels were clipped at a threshold of ± 14.6 G, ± 8.5 G, and ± 6.4 G, respectively.

shown in the composite full-disk BaSAMS in Figures 1–4) of the mature but decaying $\beta\gamma$ -region NOAA 12034, which showed minor flare activity in X-rays at the C-class level.

Varying the duration over which the background is computed affects significantly the morphology of the BaSAM (see Figure 6). We computed BaSAMS with a duration 2 to 16-hours. The significant morphological changes that are apparent cannot be attributed to sparse temporal sampling. Already for the 2-hour case, about 160 images are used to compute the BaSAM, which is sufficient to assume a Gaussian distribution for the magnetic field variation in each pixel. The longer the duration, the smoother becomes the appearance of deep magnetograms. Quiet-Sun magnetic fields become enhanced but with fuzzy boundaries. As a consequence, most fine structure is visible in BaSAMS for backgrounds with a short duration because the background did not have time to evolve. This allows us to identify areas with pronounced instantaneous magnetic field variations. In contrast, a longer duration for the background leads to larger variations of the magnetic field above a smoother background. Persistent variations stand out more clearly, which is advantageous when investigating magnetic connections within an active region or with its surroundings, *e.g.* the magnetic network (see Verma *et al.*, 2012).

Using sliding averages for the background places emphasis on instantaneous variations. The duration of the sliding averages impacts the appearance of BaSAMS as shown for the UV intensity variation over a 16-hour period (see Figure 7). The duration of the sliding average was doubled in each step from 30 min, over 60 and 120 min, to 240 min. Even though no C-class flares or larger were recorded for active region NOAA 12034 on 2014 April 17, all UV BaSAMS show clearly brightenings between opposite-polarity sunspots at a location with mixed polarities. Interestingly, these brightenings are absent around the leading sunspot. The strength of the brightenings increases with the duration of the sliding average for the same reasons mentioned above for the magnetic BaSAMS (Figure 6). For the shortest sliding averages the brightenings decompose into point-like features, indicating that small-scale flaring occurs at very localized regions, which are smeared out for longer duration sliding averages.

To quantify the differences between BaSAMS, when varying the overall duration or the duration of the sliding average for the background, the linear and rank-order

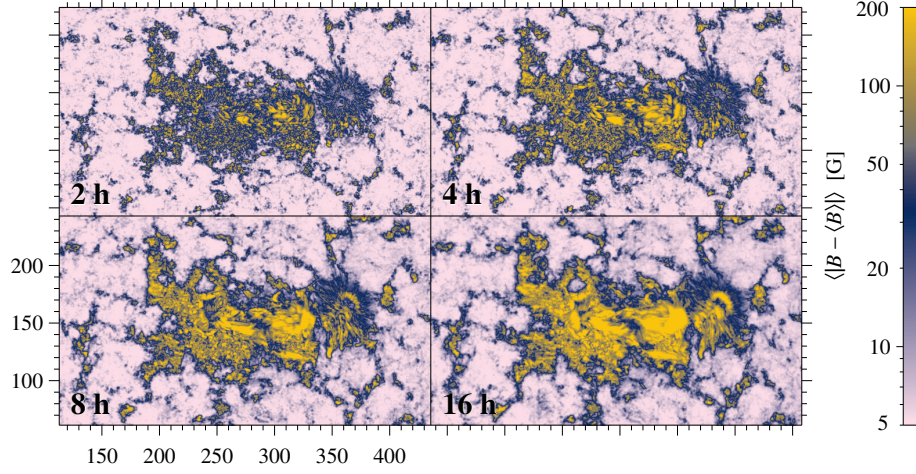


Figure 6. Magnetic BaSAMs with a different duration of the background $\langle |B - \langle B \rangle| \rangle_{2h, 4h, 8h, 16h}$ (logarithmic display) showing active region NOAA 12034 on 2014 April 17. The disc center coordinates are given in seconds of arc.

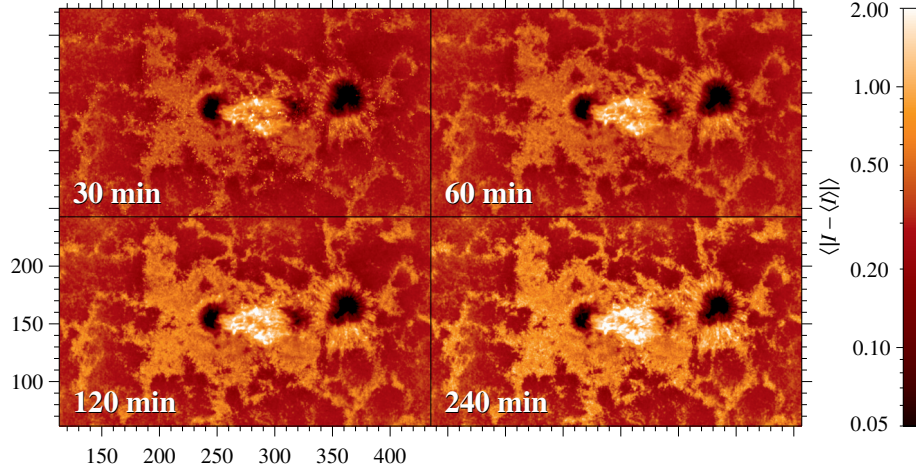


Figure 7. UV BaSAMs with a different duration of the sliding average $\langle |I - \langle I \rangle| \rangle_{30min, 60min, 120min, 240min}$ (logarithmic display) for active region NOAA 12034 (see Figure 6). The duration over which the BaSAMs were computed was 16 hours in all cases.

correlation coefficients were computed and summarized in Table 1. Linear and rank-order correlation coefficients evaluate either linear or monotonic relationships between two continuous variables, respectively. In general, the rank-order correlation is less restrictive, which is helpful if no *a priori* knowledge is available about the exact data model. However, the high values for both types of correlation coefficients indicates that a linear model represents the data well. Using the 2-hour magnetic BaSAM as reference, the correlation decreases with longer duration of the background. This decorrelation is stronger for the rank-order correlation coefficient. In addition, consecutive maps show

Table 1. Linear (*above diagonal*) and rank-order (*below diagonal*) correlation coefficients for the four BaSAMS in Figures 6 (*left*) and 7 (*right*), respectively.

	2 h	4 h	8 h	16 h		30 min	60 min	120 min	240 min
2 h		0.92	0.80	0.71	30 min		0.94	0.90	0.86
4 h	0.92		0.91	0.80	60 min	0.94		0.98	0.94
8 h	0.86	0.93		0.91	120 min	0.89	0.98		0.98
16 h	0.79	0.86	0.93		240 min	0.85	0.94	0.98	

about the same values for linear as well as rank-order correlation coefficients. The linear and rank-order correlation coefficients are about the same for the UV BaSAMS with a different duration of the sliding averages. Furthermore, the trend for the temporal decorrelation is similar to that of the magnetic BaSAMS. In summary, the overall high correlation coefficients indicate that all BaSAMS capture the general properties of temporal variations in active regions. Furthermore, the duration of the background and the duration of the sliding averages affect the fine structures contained in the BaSAMS, *i.e.* the parameters have to be adapted to the scientific objective and the observed feature on the Sun.

We present two cases illustrating that BaSAMS are applicable to smaller ROIs: (1) the flare-prolific active region NOAA 11515 and (2) the active region NOAA 12081 containing an axisymmetric sunspot. Differential rotation, CLV, and geometrical foreshortening were corrected for both ROIs (see Verma, Kummerow, and Denker, 2018). In NOAA 11515, we focus on the 24-hour time-period starting 16:00 UT on 2012 July 2 (Louis *et al.*, 2014), when the leading spot exhibited strong rotation with respect to the other sunspots in the active region. Another distinguishing property was the fast separation of the leading and trailing sunspots. This complex active region was the source of many M-class solar flares. Rotation and separation can be traced in the 24-hour BaSAMS for magnetic field and UV intensity (Figure 8). The elongated region in the central part of the ROI shows an enhanced variation of the magnetic field and UV intensity, which highlights the stretching of the active region and the separating motion of the spots. This stretching is more prominently visible in the magnetic BaSAM, where it appears as two elongated bands. The rotation of the leading sunspot becomes evident in the UV BaSAM as a bright circular feature, which encompasses three quarters of the leading sunspot, in particular in penumbra locations. Axisymmetric sunspots may not produce clear signatures of rotation in BaSAMS. However, in the presence of asymmetric features such as a rudimentary/incomplete penumbra or the collision with encircling pores as in the case of the leading sunspot in active region NOAA 11515, rotation can be detected by the BaSAM method. In particular, UV variations are caused by shear motions between leading sunspot and encircling pores, which led to continuous flickering of the UV intensity, likely related to local reconnection.

Apart from capturing splitting and shear motions in the more active regions, BaSAMS are a useful tool to investigate the connectivity of sunspots to their surroundings. Figure 9 depicts flow maps of horizontal proper motions, which were computed using UV images and magnetograms, along with the corresponding BaSAMS for active region NOAA 12081 at the time close to its meridian crossing. The horizontal

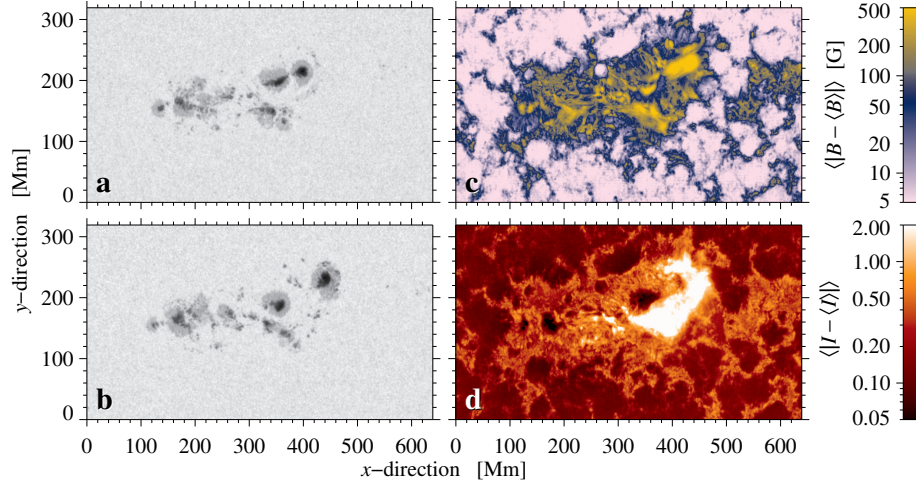


Figure 8. BaSAMS of active region NOAA 11515 for (c) magnetograms $\langle |B - \langle B \rangle| \rangle_{24h}$ and (d) UV images $\langle |I - \langle I \rangle| \rangle_{24h}$. The fast evolution of the region is evident in the continuum images observed at 16:00 UT on (a) 2012 July 2 and (b) the following day, respectively.

proper motions are estimated using LCT for the UV images and DAVE for the magnetograms. A detailed description of these two techniques that measure optical flows was presented in Verma, Kummerow, and Denker (2018). In the BaSAMS based on UV images and on magnetograms, spoke-like structures emanating from the sunspot border reach the neighboring network. These structures coincide with regions exhibiting strong outward moat flows. Hence, it becomes apparent that the sunspot and the surrounding network are part of a larger magnetic flux system, which is conjoined by plasma flows. BaSAMS make this connection visible and help to investigate the nature of the interaction between magnetic fields and plasma motions.

The availability of deep magnetograms and magnetic BaSAMS for every day since the start of the SDO mission opens the possibility to compute daily solar activity indices. The fact that about 160 magnetograms are condensed in a deep magnetogram or a magnetic BaSAM allows us to assess the contribution of persistent small-scale magnetic fields to solar activity by simple thresholding. The signal-to-noise ratio is increased in deep magnetograms by a factor of more than twelve as compared to a single magnetogram, where the noise level is about 7–12 G depending on the position on the solar disk. Using increasingly higher thresholds for deep magnetograms or BaSAMS changes the weight of quiet-Sun vs. active-region magnetic fields. In the middle panel of Figure 10, we show an activity index based on magnetic BaSAMS, where we employed a threshold of 20 G for averaging the magnetic field variations across the solar disk, *i.e.* the index provides the average variation of the magnetic field per pixel in a BaSAM. At the threshold level of 20 G, both quiet-Sun and active region magnetic fields contribute to the magnetic field variations. This approach is rather simplistic because it does not consider any geometric correction with respect to the area contained in a single pixel or regarding the magnetic field inclination. However, already at this level solar cycle properties and the solar rotation period become apparent, *e.g.* the double maximum of solar cycle No. 24.

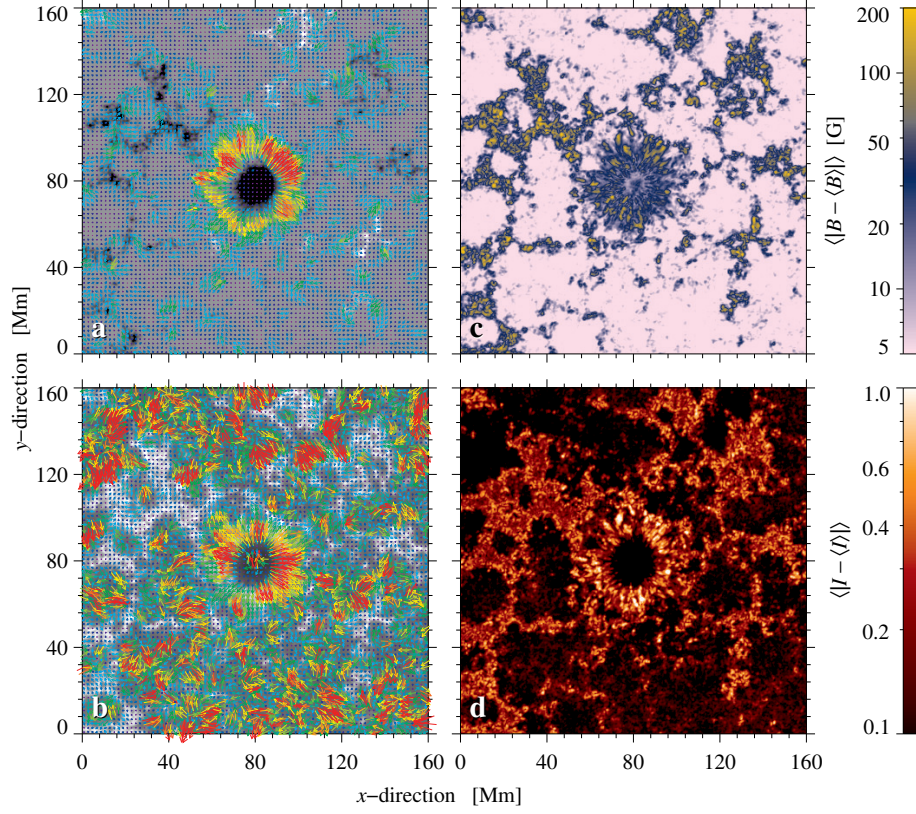


Figure 9. Axisymmetric sunspot of active region NOAA 12081 with moat flows measure using LCT and DAVE with corresponding BaSAM ROIs. The rainbow colored arrows represent the magnitude as well as direction of the horizontal proper motions. Violet and red arrows correspond to flow speeds of lower than 0.1 km s^{-1} and larger than 0.4 km s^{-1} , respectively.

The daily variation of the international sunspot number S_n is plotted in the upper panel of Figure 10 for comparison. While the sunspot number reaches zero in the absence of sunspots, *i.e.* at the beginning and end of the displayed time-series, the BaSAM index shows a distinct basal level for two reasons: (1) the presence of noise when computing the absolute mean deviation in Equation 1 and (2) the existence of ubiquitous magnetic fields on the solar surface – even at solar minimum – and their variation. In addition, the BaSAM index appears smoother because it includes all magnetic fields that are present on the solar surface and not just those that leave a visible imprint in continuum or broad-band images such as sunspots and pores. Furthermore, the definition of the sunspot number is based on the proper identification of individual sunspots and sunspot groups, which is prone to systematical errors, and results in integer values without any further subdivision. Consequently, the better statistical foundation of BaSAM activity indices makes them a good choice for time-series analysis.

The bottom panel of Figure 10 shows the one-to-one comparison of the BaSAM index and the sunspot number. Both curves are smoothed using a Gaussian kernel with

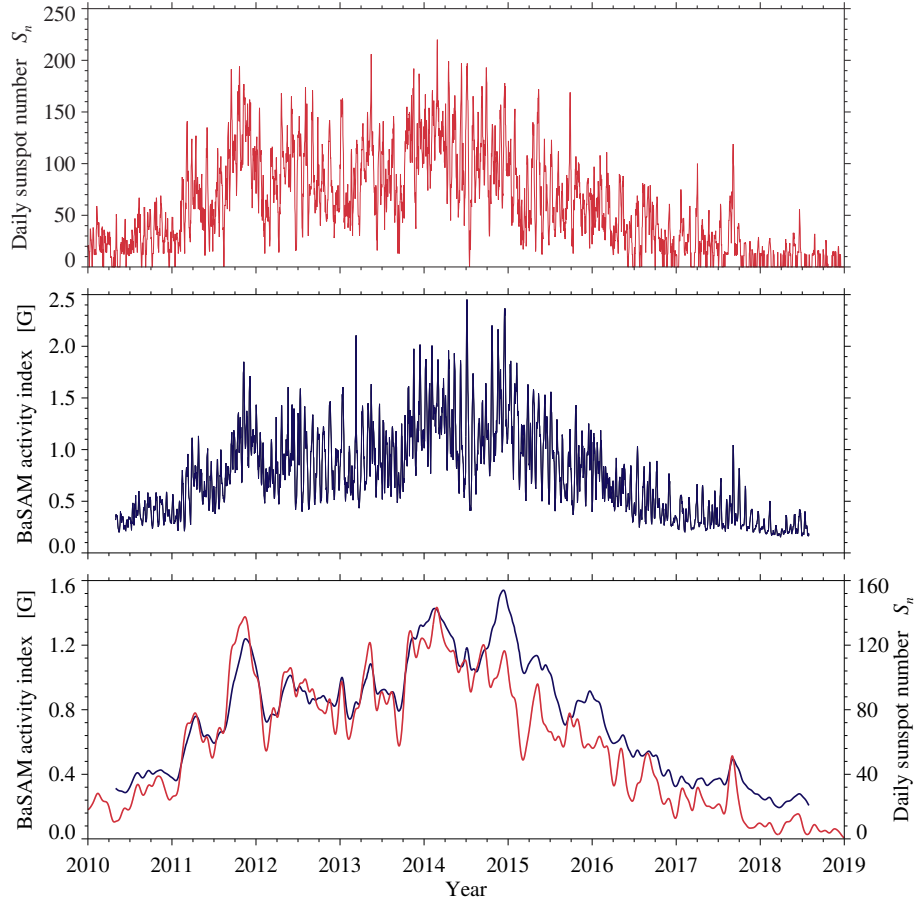


Figure 10. Variation of the daily sunspot number S_n (*top*) during the 9-year period since 2010. BaSAM activity index (*middle*) using a threshold of 20 G for averaging the magnetic field variations across the solar disk. Small-scale variations in time reflect the synodic rotation period of the Sun. In addition, the two maxima of solar cycle No. 24 are clearly visible in the BaSAM activity index. Smoothed versions (Gaussian kernel with a FWHM = 28 days) of the sunspot number (*red*) and the BaSAM index (*blue*) are displayed for direct comparison (*bottom*).

a FWHM of 28 days so that the two curves can be compared much more easily. These curves are very similar to the ones presented in Figure 3 of Morgan and Taroyan (2017) who discussed the global means for coronal temperature, emission measure (EM), and photospheric magnetic field for years 2010–2017. They found that active region temperature, EM, and magnetic field are highly correlated. In addition, they find an initial peak in early 2012 and a secondary peak in mid-2014 for some of these parameters before the maximum in 2015. These features are also present in the BaSAM index but the maximum in 2015 is missing in the daily sunspot number S_n . Interestingly, the smoothed curves track each other very well up to this point, after which the BaSAM index displays a clear offset. The nature of this offset, whether instrumental or real, still has to be investigated.

Time-series analysis using the Fourier transform of the activity index reveals a cluster of power peaks around the synodic rotation period of the Sun. The periods of the three most significant peaks are in order of significance 26.1, 28.3, and 27.2 days, respectively. At this moment, the origin of this splitting is not clear. Since the input for computing activity indices are full-disk magnetograms, computing the latitude dependence of activity indices (*e.g.* Knaack, Stenflo, and Berdyugina, 2005) or searching for active longitudes (*e.g.* Balthasar, 2007) becomes straightforward. A more detailed investigation, however, is beyond the scope of the current study and is deferred to a future publication. Such a study will also include solar activity indices based on BaSAMs of the UV intensity.

5. Discussion and Conclusions

We present a method to visualize variations of the UV intensity and magnetic field. BaSAMs are derived not only for solar full-disk data but also for smaller ROIs. The observed temporal variations are visualized in the spatial domain. In addition, the disk-integrated variation can be derived and used as an indicator of long-term solar activity changes, which can be translated into UV or magnetic activity indices. Sunspots numbers, sunspot area, and the 10.7 cm radio flux are among the commonly used indices representing long-term solar activity. Solar cycle variations are often presented in terms of Zurich sunspot numbers (*e.g.* Chernosky and Hagan, 1958). Furthermore, shape and strength of next solar cycle are often predicted in terms of sunspot numbers (Hathaway, Wilson, and Reichmann, 1999). Indices based on BaSAMs display a good correlation with the aforementioned solar activity indices and have an additional advantage, *i.e.* they can be computed for features, where the strength of the variations significantly differs. Thus, contributions of quiet-Sun and highly active regions can be separated.

BaSAMs are complementary and provide additional scientific insight to existing solar full-disk data. The shift-and-add method for short-exposure images is one of the early attempts to improve photometric accuracy while preserving fine-structure when observing through a turbulent medium such as Earth's atmosphere (Hunt, Fright, and Bates, 1983). Thus, co-adding images or magnetograms to enhance photometric accuracy or magnetic sensitivity is nothing new. For example, magnetograms reaching polarization levels of 10^{-4} can be produced with fast polarimeters and cameras in combination with post-processing (see Wang *et al.*, 1998, for an implementation at *Big Bear Solar Observatory* (BBSO)). They found that 1000 and 100 integrations are needed for quiet-Sun and active regions, respectively, to reach the accuracy of the aforementioned polarization level. We follow the same principle when creating deep magnetograms. Even though SDO data are not affected by atmospheric seeing, solar differential rotation must be nevertheless corrected before co-adding magnetograms. In our deep magnetograms, we are able to detect very weak magnetic fields in the polar and internetwork regions. Sensitive and high-cadence magnetograms are a prerequisite for the BaSAM method. For example, considering the image scale ($2'' \text{ pixel}^{-1}$), cadence (96 min), and detector technology, creating BaSAMs based on synoptic full-disk magnetograms obtained with the *Michelson Doppler Imager* (MDI, Scherrer *et al.*, 1995) on board the *Solar and Heliospheric Observatory* (SoHO, Domingo, Fleck, and Poland, 1995) was out of reach at that time.

The multiple wavelengths channels of AIA provide full-disk solar images covering various solar atmospheric layers. To extract more information from these full-disk images, Viall and Klimchuk (2012) used a property of coronal loops, where the peak intensities in cooler atmospheric layers are reached at different times than those of hotter atmospheric layers. By measuring the time lag of the intensity response in pairs of EUV channels for a duration of 24 hours, they demonstrated that the coronal plasma is very dynamic and evolves on different time scales. This time-lag method computes temporal cross-correlations of intensity profiles on a pixel-by-pixel basis using properly aligned time-series of AIA images taken in two channels. The results are maps identifying variations, periodic phenomena, and oscillations from lower to higher atmospheric layers. The BaSAM method differs from this approach because it refers to just one atmospheric layer and visualizes the accumulated strength of temporal variations. UV images and magnetograms do not just represent different data types but they also sample two different atmospheric layers, *i.e.* upper photosphere/transition region and photosphere. However, both methods serve as examples that full-disk SDO data can be used as a starting point for value-added data products such as UV and magnetic BaSAMs that complement each other.

Time-series full-disk data corrected for solar differential rotation facilitated LCT (*e.g.* Bearegard, Verma, and Denker, 2012; Verma, Kummerow, and Denker, 2018) and were the point of departure for developing the BaSAM method. Recently, Morgan and Hutton (2018) proposed a new method to follow continuous faint motions in the corona using AIA EUV images. The *Time-Normalized-Optical-Flow* (TNOF) method employs sliding averages and temporal smoothing to remove the slowly varying background from a time-series of EUV images for each pixel. The processed time-series data can then be analyzed with optical flow tracking techniques, which facilitates following coronal motions at sub-pixel resolution. However, in this case the magnitude of the variation is not decisive but its temporal evolution, which yields the motion vector at each pixel. The high quality, cadence, and spatial resolution of SDO AIA and HMI data is the *condicio sine qua non* for methods such as TNOF and BaSAM.

However, stray light degrades SDO data and affects the photometric precision, *i.e.* the readily available level 1 data are not corrected with an appropriate point spread function (PSF). Multiple approaches were suggested to estimate the stray light contamination and to correct HMI continuum and magnetograms (*e.g.* Yeo *et al.*, 2014; Couvidat *et al.*, 2016; Criscuoli, Norton, and Whitney, 2017). Only recently the deconvolved continuum images became available for download. Recently, Díaz Baso and Asensio Ramos (2018) introduced the “Enhance” method, which uses two deep neural networks to produce deconvolved and super-resolved HMI continuum and magnetograms. The neural networks are trained on MHD simulations of active regions. Future versions of BaSAM could be based on enhanced or sharpened images and magnetograms, making it easier to discriminate between contributions from small- and large-scale features to activity indices.

So far BaSAMs are only computed for full-disk UV images and magnetograms besides some smaller ROIs for case studies. A possible extension of BaSAM is to apply it to data obtained at other wavelengths that cover chromosphere, transition region, and corona. The next step, is to compute BaSAMs for high-resolution images and magnetograms. One limitation of high-resolution data is temporal and spatial coverage. In this respect, data from space missions such as *Hinode* (Kosugi *et al.*, 2007) and *Interface*

Region Imaging Spectrograph (IRIS De Pontieu *et al.*, 2014) are a good starting point because ground-based data are affected by seeing and the day-night cycle. Nevertheless, image restoration in combination with adaptive optics occasionally produces hour-long time-series with diffraction-limited quality at meter-class solar telescopes. When computing BaSAMs, we assumed the background to be quasi-stationary, which becomes questionable for high-resolution photospheric and chromospheric observations. In this case, sliding averages are more appropriate for the computation of the background. Thus, increased spatial resolution will present us with additional information. In summary, BaSAM is a powerful method to investigate the dynamic Sun in the space and time domains.

Acknowledgments SDO HMI and AIA data are provided by the Joint Science Operations Center – Science Data Processing. The international sunspot number is compiled by the *Sunspot Index and Long-term Observations* (SILSO) project of the Royal Observatory of Belgium, Brussels. We thank Drs. Rainer Arlt and Vasyi Yurchyshyn for their comments and suggestions, which helped to improve the manuscript. This study was supported by grant DE 787/5-1 of the Deutsche Forschungsgemeinschaft (DFG) and by the European Commission’s Horizons 2020 Program under grant agreement Number 824064 (ESCAPE – European Science Cluster of Astronomy & Particle physics ESFRI research infrastructures).

Disclosure of Potential Conflicts of Interest The authors declare that they have no conflicts of interest.

References

- Aschwanden, M.J., Newmark, J.S., Delaboudinière, J.P., Neupert, W.M., Klimchuk, J.A., Gary, G.A., Portier-Fozzani, F., Zucker, A.: 1999, Three-dimensional Stereoscopic Analysis of Solar Active Region Loops. I. SOHO/EIT Observations at Temperatures of $(1.0–1.5) \times 10^6$ K. *Astrophys. J.* **515**, 842–867. doi:[10.1086/307036](https://doi.org/10.1086/307036).
- Balthasar, H.: 2007, Rotational Periodicities in Sunspot Relative Numbers. *Astron. Astrophys.* **471**, 281–287. doi:[10.1051/0004-6361:20077475](https://doi.org/10.1051/0004-6361:20077475).
- Beauregard, L., Verma, M., Denker, C.: 2012, Horizontal Flows Concurrent with an X2.2 Flare in the Active Region NOAA 11158. *Astron. Nachr.* **333**, 125–130. doi:[10.1002/asna.201111631](https://doi.org/10.1002/asna.201111631).
- Bumba, V., Howard, R.: 1965, Large-scale Distribution of Solar Magnetic Fields. *Astrophys. J.* **141**, 1502–1512. doi:[10.1086/148238](https://doi.org/10.1086/148238).
- Chernosky, E.J., Hagan, M.P.: 1958, The Zurich Sunspot Number and its Variations for 1700–1957. *J. Geophys. Res.* **63**, 775–788. doi:[10.1029/JZ063i004p00775](https://doi.org/10.1029/JZ063i004p00775).
- Couvidat, S., Schou, J., Hoeksema, J.T., Bogart, R.S., Bush, R.I., Duvall, T.L., Liu, Y., Norton, A.A., Scherrer, P.H.: 2016, Observables Processing for the Helioseismic and Magnetic Imager Instrument on the Solar Dynamics Observatory. *Solar Phys.* **291**, 1887–1938. doi:[10.1007/s11207-016-0957-3](https://doi.org/10.1007/s11207-016-0957-3).
- Criscuolo, S., Norton, A., Whitney, T.: 2017, Photometric Properties of Network and Faculae Derived from HMI Data Compensated for Scattered Light. *Astrophys. J.* **847**, 93. doi:[10.3847/1538-4357/aa8ad7](https://doi.org/10.3847/1538-4357/aa8ad7).
- De Pontieu, B., Title, A.M., Lemen, J.R., Kushner, G.D., Akin, D.J., Allard, B., Berger, T., Boerner, P., Cheung, M., Chou, C., Drake, J.F., Duncan, D.W., Freeland, S., Heyman, G.F., Hoffman, C., Hurlburt, N.E., Lindgren, R.W., Mathur, D., Rehse, R., Sabolish, D., Seguin, R., Schrijver, C.J., Tarbell, T.D., Wülser, J.P., Wolfson, C.J., Yanari, C., Mudge, J., Nguyen-Phuc, N., Timmons, R., van Bezooijen, R., Weingrod, I., Brookner, R., Butcher, G., Dougherty, B., Eder, J., Knagenhjelm, V., Larsen, S., Mansir, D., Phan, L., Boyle, P., Cheimets, P.N., DeLuca, E.E., Golub, L., Gates, R., Hertz, E., McKillop, S., Park, S., Perry, T., Podgorski, W.A., Reeves, K., Saar, S., Testa, P., Tian, H., Weber, M., Dunn, C., Eccles, S., Jaeggli, S.A., Kankelborg, C.C., Mashburn, K., Pust, N., Springer, L., Carvalho, R., Kleint, L., Marmie, J., Mazmanian, E., Pereira, T.M.D., Sawyer, S., Strong, J., Worden, S.P., Carlsson, M., Hansteen, V.H., Leenaarts, J., Wiesmann, M., Aloise, J., Chu, K.C., Bush, R.I., Scherrer, P.H., Brekke, P., Martinez-Sykora, J., Lites, B.W., McIntosh, S.W., Uitenbroek, H., Okamoto, T.J., Gumm, M.A., Auker, G., Jerram, P., Pool, P., Waltham, N.: 2014, The Interface Region Imaging Spectrograph (IRIS). *Solar Phys.* **289**, 2733–2779. doi:[10.1007/s11207-014-0485-y](https://doi.org/10.1007/s11207-014-0485-y).
- de Toma, G., White, O.R., Harvey, K.L.: 2000, A Picture of Solar Minimum and the Onset of Solar Cycle 23. I. Global Magnetic Field Evolution. *Astrophys. J.* **529**, 1101–1114. doi:[10.1086/308299](https://doi.org/10.1086/308299).

- Denker, C., Johannesson, A., Marquette, W., Goode, P.R., Wang, H., Zirin, H.: 1999, Synoptic $H\alpha$ Full-Disk Observations of the Sun from Big Bear Solar Observatory. I. Instrumentation, Image Processing, Data Products, and First Results. *Solar Phys.* **184**, 87–102. doi:[10.1023/A:1005047906097](https://doi.org/10.1023/A:1005047906097).
- Díaz Baso, C.J., Asensio Ramos, A.: 2018, Enhancing SDO/HMI Images Using Deep Learning. *Astron. Astrophys.* **614**, A5. doi:[10.1051/0004-6361/201731344](https://doi.org/10.1051/0004-6361/201731344).
- Domingo, V., Fleck, B., Poland, A.I.: 1995, The SOHO Mission: An Overview. *Solar Phys.* **162**, 1–37. doi:[10.1007/BF00733425](https://doi.org/10.1007/BF00733425).
- Freeland, S.L., Handy, B.N.: 1998, Data Analysis with the SolarSoft System. *Solar Phys.* **182**, 497–500. doi:[10.1023/A:1005038224881](https://doi.org/10.1023/A:1005038224881).
- Gaizauskas, V., Harvey, K.L., Harvey, J.W., Zwaan, C.: 1983, Large-scale Patterns Formed by Solar Active Regions During the Ascending Phase of Cycle 21. *Astrophys. J.* **265**, 1056–1065. doi:[10.1086/160747](https://doi.org/10.1086/160747).
- Hathaway, D.H., Wilson, R.M., Reichmann, E.J.: 1999, A Synthesis of Solar Cycle Prediction Techniques. *J. Geophys. Res.* **104**, 22375–22388. doi:[10.1029/1999JA900313](https://doi.org/10.1029/1999JA900313).
- Howard, R.F., Harvey, J.W., Forgach, S.: 1990, Solar Surface Velocity Fields Determined from Small Magnetic Features. *Solar Phys.* **130**, 295–311. doi:[10.1007/BF00156795](https://doi.org/10.1007/BF00156795).
- Hunt, B.R., Fright, W.R., Bates, R.H.T.: 1983, Analysis of the Shift-and-Add Method for Imaging through Turbulent Media. *J. Opt. Soc. Am.* **73**, 456–465. doi:[10.1364/JOSA.73.000456](https://doi.org/10.1364/JOSA.73.000456).
- Knaack, R., Stenflo, J.O., Berdyugina, S.V.: 2005, Evolution and Rotation of Large-scale Photospheric Magnetic Fields of the Sun during Cycles 21–23. Periodicities, North-South Asymmetries and r -Mode Signatures. *Astron. Astrophys.* **438**, 1067–1082. doi:[10.1051/0004-6361:20042091](https://doi.org/10.1051/0004-6361:20042091).
- Kosugi, T., Matsuzaki, K., Sakao, T., Shimizu, T., Sone, Y., Tachikawa, S., Hashimoto, T., Minesugi, K., Ohnishi, A., Yamada, T., Tsuneta, S., Hara, H., Ichimoto, K., Suematsu, Y., Shimojo, M., Watanabe, T., Shimada, S., Davis, J.M., Hill, L.D., Owens, J.K., Title, A.M., Culhane, J.L., Harra, L.K., Doschek, G.A., Golub, L.: 2007, The Hinode (Solar-B) Mission: An Overview. *Solar Phys.* **243**, 3–17. doi:[10.1007/s11207-007-9014-6](https://doi.org/10.1007/s11207-007-9014-6).
- Kummerow, P.: 2015, Vermessung der Horizontalen Strömungen in Sonnenflecken. Master's thesis, Universität Potsdam.
- Lemen, J.R., Title, A.M., Akin, D.J., Boerner, P.F., Chou, C., Drake, J.F., Duncan, D.W., Edwards, C.G., Friedlaender, F.M., Heyman, G.F., Hurlburt, N.E., Katz, N.L., Kushner, G.D., Levay, M., Lindgren, R.W., Mathur, D.P., McFeaters, E.L., Mitchell, S., Rehse, R.A., Schrijver, C.J., Springer, L.A., Stern, R.A., Tarbell, T.D., Wuelser, J.P., Wolfson, C.J., Yanari, C., Bookbinder, J.A., Cheimets, P.N., Caldwell, D., Deluca, E.E., Gates, R., Golub, L., Park, S., Podgorski, W.A., Bush, R.I., Scherrer, P.H., Gumm, M.A., Smith, P., Auker, G., Jerram, P., Pool, P., Soufli, R., Windt, D.L., Beardsley, S., Clapp, M., Lang, J., Waltham, N.: 2012, The Atmospheric Imaging Assembly (AIA) on the Solar Dynamics Observatory (SDO). *Solar Phys.* **275**, 17–40. doi:[10.1007/s11207-011-9776-8](https://doi.org/10.1007/s11207-011-9776-8).
- Lin, H., Rimmele, T.: 1999, The Granular Magnetic Fields of the Quiet Sun. *Astrophys. J.* **514**, 448–455. doi:[10.1086/306925](https://doi.org/10.1086/306925).
- Louis, R.E., Puschmann, K.G., Kliem, B., Balthasar, H., Denker, C.: 2014, Sunspot Splitting Triggering an Eruptive Flare. *Astron. Astrophys.* **562**, A110. doi:[10.1051/0004-6361/201321106](https://doi.org/10.1051/0004-6361/201321106).
- Morgan, H., Hutton, J.: 2018, Ubiquitous and Continuous Propagating Disturbances in the Solar Corona. *Astrophys. J.* **853**, 145. doi:[10.3847/1538-4357/aaa4b9](https://doi.org/10.3847/1538-4357/aaa4b9).
- Morgan, H., Taroyan, Y.: 2017, Global Conditions in the Solar Corona from 2010 to 2017. *Sci. Adv.* **3**, e1602056. doi:[10.1126/sciadv.1602056](https://doi.org/10.1126/sciadv.1602056).
- November, L.J., Simon, G.W.: 1988, Precise Proper-motion Measurement of Solar Granulation. *Astrophys. J.* **333**, 427–442. doi:[10.1086/166758](https://doi.org/10.1086/166758).
- Pesnell, W.D., Thompson, B.J., Chamberlin, P.C.: 2012, The Solar Dynamics Observatory (SDO). *Solar Phys.* **275**, 3–15. doi:[10.1007/s11207-011-9841-3](https://doi.org/10.1007/s11207-011-9841-3).
- Pierce, A.K., Slaughter, C.D.: 1977, Solar Limb Darkening. I. $\lambda\lambda(3033-7297)$. *Solar Phys.* **51**, 25–41. doi:[10.1007/BF00240442](https://doi.org/10.1007/BF00240442).
- Pierce, A.K., Slaughter, C.D., Weinberger, D.: 1977, Solar Limb Darkening in the Interval 7404–24018 Å, II. *Solar Phys.* **52**, 179–189. doi:[10.1007/BF00935800](https://doi.org/10.1007/BF00935800).
- Roupe van der Voort, L.H.M., Rutten, R.J., Sütterlin, P., Sloover, P.J., Krijger, J.M.: 2003, La Palma Observations of Umbral Flashes. *Astron. Astrophys.* **403**, 277–285. doi:[10.1051/0004-6361:20030237](https://doi.org/10.1051/0004-6361:20030237).
- Scherrer, P.H., Bogart, R.S., Bush, R.I., Hoeksema, J.T., Kosovichev, A.G., Schou, J., Rosenberg, W., Springer, L., Tarbell, T.D., Title, A., Wolfson, C.J., Zayer, I., MDI Engineering Team: 1995, The Solar Oscillations Investigation – Michelson Doppler Imager. *Solar Phys.* **162**, 129–188. doi:[10.1007/BF00733429](https://doi.org/10.1007/BF00733429).
- Scherrer, P.H., Schou, J., Bush, R.I., Kosovichev, A.G., Bogart, R.S., Hoeksema, J.T., Liu, Y., Duvall, T.L., Zhao, J., Title, A.M., Schrijver, C.J., Tarbell, T.D., Tomczyk, S.: 2012, The Helioseismic and Magnetic Imager (HMI) Investigation for the Solar Dynamics Observatory (SDO). *Solar Phys.* **275**, 207–227. doi:[10.1007/s11207-011-9834-2](https://doi.org/10.1007/s11207-011-9834-2).

- Schou, J., Scherrer, P.H., Bush, R.I., Wachter, R., Couvidat, S., Rabello-Soares, M.C., Bogart, R.S., Hoeksema, J.T., Liu, Y., Duvall, T.L., Akin, D.J., Allard, B.A., Miles, J.W., Rairden, R., Shine, R.A., Tarbell, T.D., Title, A.M., Wolfson, C.J., Elmore, D.F., Norton, A.A., Tomczyk, S.: 2012, Design and Ground Calibration of the Helioseismic and Magnetic Imager (HMI) Instrument on the Solar Dynamics Observatory (SDO). *Solar Phys.* **275**, 229–259. doi:[10.1007/s11207-011-9842-2](https://doi.org/10.1007/s11207-011-9842-2).
- Schuck, P.W.: 2005, Local Correlation Tracking and the Magnetic Induction Equation. *Astrophys. J. Lett.* **632**, L53–L56. doi:[10.1086/497633](https://doi.org/10.1086/497633).
- Schuck, P.W.: 2006, Tracking Magnetic Footpoints with the Magnetic Induction Equation. *Astrophys. J.* **646**, 1358–1391. doi:[10.1086/505015](https://doi.org/10.1086/505015).
- Shine, R.A., Simon, G.W., Hurlburt, N.E.: 2000, Supergranule and Mesogranule Evolution. *Solar Phys.* **193**, 313–331. doi:[10.1023/A:1005207625696](https://doi.org/10.1023/A:1005207625696).
- Snodgrass, H.B., Ulrich, R.K.: 1990, Rotation of Doppler Features in the Solar Photosphere. *Astrophys. J.* **351**, 309–316. doi:[10.1086/168467](https://doi.org/10.1086/168467).
- Title, A.M., Tarbell, T.D., Acton, L., Duncan, D., Simon, G.W.: 1986, White-light Movies of the Solar Photosphere from the SOUP Instrument on Spacelab. *Adv. Space Res.* **6**, 253–262. doi:[10.1016/0273-1177\(86\)90447-3](https://doi.org/10.1016/0273-1177(86)90447-3).
- Verma, M., Denker, C.: 2011, Horizontal Flow Fields Observed in Hinode G-Band Images. I. Methods. *Astron. Astrophys.* **529**, A153. doi:[10.1051/0004-6361/201016358](https://doi.org/10.1051/0004-6361/201016358).
- Verma, M., Denker, C.: 2012, Horizontal Flow Fields Observed in Hinode G-band Images. III. The Decay of a Satellite Sunspot and the Role of Magnetic Flux Removal in Flaring. *Astron. Astrophys.* **545**, A192. doi:[10.1051/0004-6361/201219694](https://doi.org/10.1051/0004-6361/201219694).
- Verma, M., Kummerow, P., Denker, C.: 2018, On the Extent of the Moat Flow in Axisymmetric Sunspots. *Astron. Nachr.* **339**, 268–276. doi:[10.1002/asna.201813482](https://doi.org/10.1002/asna.201813482).
- Verma, M., Balthasar, H., Deng, N., Liu, C., Shimizu, T., Wang, H., Denker, C.: 2012, Horizontal Flow Fields Observed in Hinode G-band Images. II. Flow Fields in the Final Stages of Sunspot Decay. *Astron. Astrophys.* **538**, A109. doi:[10.1051/0004-6361/201117842](https://doi.org/10.1051/0004-6361/201117842).
- Verma, M., Denker, C., Balthasar, H., Kuckein, C., González Manrique, S.J., Sobotka, M., Bello González, N., Hoch, S., Diercke, A., Kummerow, P., Berkefeld, T., Collados, M., Feller, A., Hofmann, A., Kneer, F., Lagg, A., Löhner-Böttcher, J., Nicklas, H., Pastor Yabar, A., Schlichenmaier, R., Schmidt, D., Schmidt, W., Schubert, M., Sigwarth, M., Solanki, S., Soltau, D., Strassmeier, K.G., Volkmer, R., von der Lühe, O., Waldmann, T.: 2016, Horizontal Flow Fields in and around a Small Active Region. The Transition Period between Flux Emergence and Decay. *Astron. Astrophys.* **596**, A3. doi:[10.1051/0004-6361/201628380](https://doi.org/10.1051/0004-6361/201628380).
- Viall, N.M., Klimchuk, J.A.: 2012, Evidence for Widespread Cooling in an Active Region Observed with the SDO Atmospheric Imaging Assembly. *Astrophys. J.* **753**, 35. doi:[10.1088/0004-637X/753/1/35](https://doi.org/10.1088/0004-637X/753/1/35).
- Wang, H., Denker, C., Spirock, T., Goode, P.R., Yang, S., Marquette, W., Varsik, J., Fear, R.J., Nenow, J., Dingley, D.D.: 1998, New Digital Magnetograph at Big Bear Solar Observatory. *Solar Phys.* **183**, 1–13. doi:[10.1023/A:1005027605781](https://doi.org/10.1023/A:1005027605781).
- Wang, Y., Noyes, R.W., Tarbell, T.D., Title, A.M.: 1995, Vorticity and Divergence in the Solar Photosphere. *Astrophys. J.* **447**, 419–427. doi:[10.1086/175886](https://doi.org/10.1086/175886).
- Welsch, B.T., Kusano, K., Yamamoto, T.T., Muglach, K.: 2012, Decorrelation Times of Photospheric Fields and Flows. *Astrophys. J.* **747**, 130. doi:[10.1088/0004-637X/747/2/130](https://doi.org/10.1088/0004-637X/747/2/130).
- Yeo, K.L., Feller, A., Solanki, S.K., Couvidat, S., Danilovic, S., Krivova, N.A.: 2014, Point Spread Function of SDO/HMI and the Effects of Stray Light Correction on the Apparent Properties of Solar Surface Phenomena. *Astron. Astrophys.* **561**, A22. doi:[10.1051/0004-6361/201322502](https://doi.org/10.1051/0004-6361/201322502).